Handout 2: relic gravitational waves

In the early universe, primordial magnetic fields are likely of sufficient energy that the associated stress, B_iB_j, must have driven relic gravitational waves. They would not have (much) decayed since their generation, so their detection would reveal an independent picture of what happened early on.

1 GW equation with conformal time

In physical units, the prefactor on the stress in the linearized GW equation is $16\pi G/c^2$. Here, however, we focus on the scale factor and postpone this aspect, so we put the prefactor to unity. Likewise, the traceless-transverse projection will be discussed separately. The GW equation then reads

$$\frac{\partial^2 h_{\rm phys}}{\partial t_{\rm phys}^2}+3H\frac{\partial h_{\rm phys}}{\partial t_{\rm phys}}-\nabla_{\rm phys}^2 h_{\rm phys}=T_{\rm phys} \tag{1}$$

where $h_{\rm phys}=h/a$ and

$$\frac{\partial}{\partial t_{\rm phys}}=\frac{1}{a}\frac{\partial}{\partial t},\quad \nabla_{\rm phys}^2=\frac{1}{a^2}\nabla^2 \tag{2}$$

Compute

$$\frac{\partial h_{\rm phys}}{\partial t_{\rm phys}}=\frac{1}{a}\frac{\partial}{\partial t}(a^{-1}h)=-\frac{\dot a}{a^3}h+\frac{\dot h}{a^2} \tag{3}$$

and

$$\frac{\partial^2 h_{\rm phys}}{\partial t_{\rm phys}^2}=\frac{1}{a}\frac{\partial}{\partial t}\left(-\frac{\dot a}{a^3}h+\frac{\dot h}{a^2}\right) \tag{4}$$

so

$$\frac{\partial^2 h_{\rm phys}}{\partial t_{\rm phys}^2}=-\frac{\ddot a}{a^4}h+3\frac{\dot a^2}{a^5}h-\frac{\dot a}{a^4}\dot h+\frac{\ddot h}{a^3}-2\frac{\dot a}{a^4}\dot h \tag{5}$$

or

$$\frac{\partial^2 h_{\rm phys}}{\partial t_{\rm phys}^2}=-\frac{\ddot a}{a^4}h+3\frac{\dot a^2}{a^5}h-3\frac{\dot a}{a^4}\dot h+\frac{\ddot h}{a^3} \tag{6}$$

Since $H=\dot a/a^2$, we have

$$\begin{aligned}&\frac{\partial^2 h_{\rm phys}}{\partial t_{\rm phys}^2}+3H\frac{\partial h_{\rm phys}}{\partial t_{\rm phys}} \\ &=-\frac{\ddot a}{a^4}h+3\frac{\dot a^2}{a^5}h-3\frac{\dot a}{a^4}\dot h+\frac{\ddot h}{a^3}-3\frac{\dot a^2}{a^5}h+3\frac{\dot a}{a^4}\dot h\end{aligned} \tag{7}$$

so

$$\frac{\partial^2 h_{\rm phys}}{\partial t_{\rm phys}^2}+3H\frac{\partial h_{\rm phys}}{\partial t_{\rm phys}}=-\frac{\ddot a}{a^4}h+\frac{\ddot h}{a^3} \tag{8}$$

Since $T_{\rm phys}=T/a^4$, the GW equation becomes

$$-\frac{\ddot a}{a^4}h+\frac{\ddot h}{a^3}-\frac{1}{a^3}\nabla^2 h=\frac{T}{a^4} \tag{9}$$

or

$$\ddot h-\frac{\ddot a}{a}h-\nabla^2 h=\frac{T}{a} \tag{10}$$

and therefore

$$\ddot{h} - \left(\frac{\ddot{a}}{a} + \nabla^2\right) h = \frac{T}{a}. \tag{11}$$

In Fourier space, we have

$$\ddot{\tilde{h}} - \left(\frac{\ddot{a}}{a} - k^2\right) \tilde{h} = \frac{\tilde{T}}{a}, \tag{12}$$

so we see that the effective wavenumber becomes imaginary when $\ddot{a}/a > k^2$. This effect destabilizes long wavelengths and is important during inflation.

We recall here that dots denote derivatives with respect to *conformal time*. During the radiation era, a grows linearly, so $\ddot{a} = 0$, i.e.,

$$\ddot{\tilde{h}} + k^2 \tilde{h} = \frac{\tilde{T}}{a}, \tag{13}$$

and the only effect of expansion lies in the $1/a$ dilution factor in the source.

2 The prefactor

With the prefactor included, we have

$$\ddot{\tilde{h}} + c^2 k^2 \tilde{h} = \frac{16\pi G}{c^2} \frac{\tilde{T}}{a}. \tag{14}$$

As noted above, the critical density is given by $\rho_{\rm crit} = 3H^2/8\pi G$. Therefore, we have

$$\ddot{\tilde{h}} + c^2 k^2 \tilde{h} = \frac{16\pi G}{c^2} \frac{3H^2}{8\pi G} \frac{\tilde{T}/\rho_{\rm crit}}{a}. \tag{15}$$

or

$$\left(\frac{{\rm d}^2}{{\rm d}(Ht)^2} + \frac{c^2 k^2}{H^2}\right) \tilde{h} = \frac{6\tilde{T}}{\rho_{\rm crit} c^2 a}. \tag{16}$$

In the early universe, the radiation energy is approximately equal to the critical density. Therefore, it is convenient to solve the hydrodynamic equations in units where $\rho_{\rm crit} = c^2 = 1$ and to normalize time by the initial value of $1/H$. The final set of equations is therefore

$$\left(\frac{{\rm d}^2}{{\rm d}\bar{t}^2} + \bar{k}^2\right) \tilde{h} = \frac{6\tilde{\bar{T}}}{\bar{t}}, \tag{17}$$

and to omit the overbars from now on.

2.1 TT projection and linear polarization basis

The six components of the spatial part of the symmetric tensor $h_{ij}(\boldsymbol{x}, t)$, characterizing the linearized evolution of the scaled strains, contain four degrees of gauge freedom. In the TT gauge, these are eliminated by requiring $\tilde{h}^{\rm TT}_{ij}(\boldsymbol{k}, t)$ to be a transverse and traceless tensor, i.e., $\tilde{h}^{\rm TT}_{ii}(\boldsymbol{k}, t) = 0$, and $k_j \tilde{h}^{\rm TT}_{ij}(\boldsymbol{k}, t) = 0$, respectively, where Einstein summation convention is being used, leaving only two independent components which, in the linear polarization basis, are the + and × polarization modes. To compute the physically observable characteristic amplitude, GW energy density, and the degree of circular polarization, we compute $\tilde{h}^{\rm TT}_{ij}(\boldsymbol{k}, t)$ and $\tilde{h}'^{\rm TT}_{ij}(\boldsymbol{k}, t)$, and express them in terms of the linear polarization modes. To compute $\tilde{h}^{\rm TT}_{ij}(\boldsymbol{k}, t)$ from $h_{ij}(\boldsymbol{x}, t)$, we take the Fourier transform of the six components of $h_{ij}(\boldsymbol{x}, t)$ using the convention

$$\tilde{h}_{ij}(\boldsymbol{k}, t) \;=\; \int h_{ij}(\boldsymbol{x}, t)\, e^{-{\rm i}\boldsymbol{k}\cdot\boldsymbol{x}}\, {\rm d}^3\boldsymbol{x}\,, \tag{18}$$

for $1 \le i \le j \le 3$ and compute the components in the TT gauge as

$$\tilde{h}_{ij}^{\rm TT}(\boldsymbol{k},t) \,=\, (P_{il}P_{jm} - \tfrac{1}{2}P_{ij}P_{lm})\,\tilde{h}_{lm}(\boldsymbol{k},t)\,. \tag{19}$$

Next, we compute the linear polarization basis,

$$e_{ij}^{+}(\boldsymbol{k}) \,=\, e_i^1 e_j^1 - e_i^2 e_j^2\,, \qquad e_{ij}^{\times}(\boldsymbol{k}) \,=\, e_i^1 e_j^2 + e_i^2 e_j^1\,, \tag{20}$$

where $\boldsymbol{e}^1$ and $\boldsymbol{e}^2$ are unit vectors perpendicular to $\boldsymbol{k}$ and perpendicular to each other. This polarization basis has the following orthogonality property

$$e_{ij}^{+}(\boldsymbol{k})e_{ij}^{+}(\boldsymbol{k}) \,=\, e_{ij}^{\times}(\boldsymbol{k})e_{ij}^{\times}(\boldsymbol{k}) \,=\, 2\,, \qquad e_{ij}^{+}(\boldsymbol{k})e_{ij}^{\times}(\boldsymbol{k}) \,=\, 0\,. \tag{21}$$

Thus, the strains are decomposed into the two independent + and × modes, such that $\tilde{h}_{ij}^{\rm TT}(\boldsymbol{k},t) = e_{ij}^{+}(\boldsymbol{k})\tilde{h}_{+}(\boldsymbol{k},t) + e_{ij}^{\times}(\boldsymbol{k})\tilde{h}_{\times}(\boldsymbol{k},t)$, with

$$\tilde{h}_{+}(\boldsymbol{k},t) \,=\, \tfrac{1}{2}e_{ij}^{+}(\boldsymbol{k})\,\tilde{h}_{ij}^{\rm TT}(\boldsymbol{k},t)\,, \qquad \tilde{h}_{\times}(\boldsymbol{k},t) \,=\, \tfrac{1}{2}e_{ij}^{\times}(\boldsymbol{k})\,\tilde{h}_{ij}^{\rm TT}(\boldsymbol{k},t)\,. \tag{22}$$

We then return into physical space and compute

$$h_{+,\times}(\boldsymbol{x},t) \,=\, \frac{1}{(2\pi)^3}\int \tilde{h}_{+,\times}(\boldsymbol{k},t)\,e^{{\rm i}\boldsymbol{k}\cdot\boldsymbol{x}}\,{\rm d}^3\boldsymbol{k}\,. \tag{23}$$

Analogous calculations are performed to compute $\tilde{h}'_{+,\times}(\boldsymbol{k},t)$ and $\tilde{T}_{+,\times}(\boldsymbol{k},t)$. The normalized GW Equation (**??**) can be expressed for the two independent $+,\times$ modes, in Fourier space, as

$$\left(\frac{\partial^2}{\partial t^2} + \boldsymbol{k}^2\right)\tilde{h}_{+,\times}(\boldsymbol{k},t) \,=\, \frac{6}{t}\tilde{T}_{+,\times}(\boldsymbol{k},t)\,. \tag{24}$$

A possible choice of unit vectors in Fourier space is described in the footnote.[1]

3 GWs for a Beltrami field

It is useful to have an analytic solution to compare the numerical solutions against. A simple example that has not previously been discussed in this context is the case of GWs generated by a magnetic Beltrami

[1]The linear polarization basis is formed by $\boldsymbol{e}^1$, $\boldsymbol{e}^2$, and $\boldsymbol{e}^3 = \hat{\boldsymbol{k}}$, for all wavevectors except $\boldsymbol{k} = \boldsymbol{0}$, that corresponds to a monochromatic uniform field, and is neglected in GW spectra because uniform fields do not generate GWs. To construct $\boldsymbol{e}^1$ and $\boldsymbol{e}^2$ from $\boldsymbol{k}$, we distinguish three cases: for $|k_1| < \min(|k_2|,|k_3|)$:

$$\boldsymbol{e}^1 \,=\, {\rm sgn}\,(\boldsymbol{k})\,(0,-\hat{k}_3,\hat{k}_2)\,, \quad \boldsymbol{e}^2 \,=\, (\hat{k}_2^2+\hat{k}_3^2,-\hat{k}_1\hat{k}_2,-\hat{k}_1\hat{k}_3)\,, \tag{25}$$

for $|k_2| < \min(|k_3|,|k_1|)$:

$$\boldsymbol{e}^1 \,=\, {\rm sgn}\,(\boldsymbol{k})\,(\hat{k}_3,0,-\hat{k}_1)\,, \quad \boldsymbol{e}^2 \,=\, (-\hat{k}_2\hat{k}_1,\hat{k}_3^2+\hat{k}_1^2,-\hat{k}_2\hat{k}_3)\,, \tag{26}$$

for $|k_3| \le \min(|k_1|,|k_2|)$:

$$\boldsymbol{e}^1 \,=\, {\rm sgn}\,(\boldsymbol{k})\,(-\hat{k}_2,\hat{k}_1,0)\,, \quad \boldsymbol{e}^2 \,=\, (-\hat{k}_3\hat{k}_1,-\hat{k}_3\hat{k}_2,\hat{k}_1^2+\hat{k}_2^2)\,, \tag{27}$$

where we define the sign of a general wavevector $\boldsymbol{k} = (k_1,k_2,k_3)$ in the following way

$${\rm sgn}\,(\boldsymbol{k}) = \begin{cases} {\rm sgn}\,(k_3) & \text{if} \quad k_3 \neq 0\,, \\ {\rm sgn}\,(k_2) & \text{if} \quad k_3 = 0 \quad \text{and} \quad k_2 \neq 0\,, \\ {\rm sgn}\,(k_1) & \text{if} \quad k_2 = k_3 = 0\,, \end{cases} \tag{28}$$

such that half of the wavevectors are considered positive and the other corresponding half of the wavevectors are considered negative. The way to choose which half of the wavevectors are positive is arbitrary and could be changed leading to the same final result.

Note that neither $\boldsymbol{e}^1$ nor $\boldsymbol{e}^2$ flip sign under the parity transformation $\boldsymbol{k} \to -\boldsymbol{k}$. The reason for the ${\rm sgn}\,(\boldsymbol{k})$ term is the following. The linear polarization tensorial basis $e_{ij}^{+}(\boldsymbol{k})$ and $e_{ij}^{\times}(\boldsymbol{k})$ must be represented by even operators with respect to $\boldsymbol{k}$ to reproduce the required modes, as will be shown in next section with a simple example, a one-dimensional Beltrami field. Alternatively, without loss of generality, we could have defined $\boldsymbol{e}^1$ and $\boldsymbol{e}^2$ such that both flip sign under $\boldsymbol{k} \to -\boldsymbol{k}$ transformations, such that both $e_{ij}^{+}(\boldsymbol{k})$ and $e_{ij}^{\times}(\boldsymbol{k})$ tensors are even operators.

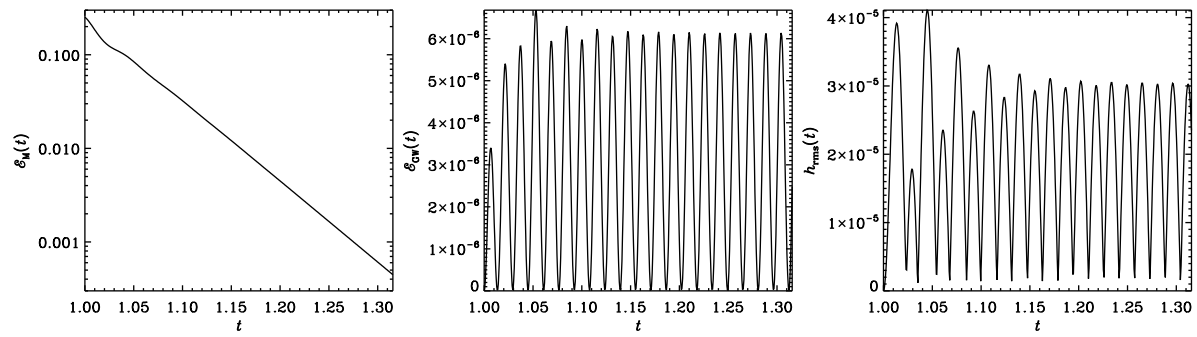

Figure 1: Magnetic energy $\mathcal{E}_{\rm M}$, gravitational wave energy $\mathcal{E}_{\rm GW}$, and rms strain $h_{\rm rms}$ versus time for the Beltrami magnetic field as initial condition.

field in a non-expanding flat universe, in the absence of fluid motions. In this case, the scale factor, $a(t)$, does not affect the GW equation. Hence, the initial time can be chosen to be zero. The one-dimensional Beltrami magnetic field is expressed as

$$\boldsymbol{B}(x,t) \;=\; B_0\Theta(t)\begin{pmatrix}0\\ \sin k_0x\\ \cos k_0x\end{pmatrix}, \tag{29}$$

where k_0 and B_0 are the characteristic wavenumber and amplitude of the Beltrami field, respectively, and $\Theta(t)$ is the Heaviside step function, such that the sourcing magnetic field is assumed to appear abruptly at the starting time of generation $t_*=0$. In the present work, we assume this time to be at the electroweak phase transition. The normalized magnetic energy density, $\Omega_{\rm M}=B_0^2/(2\mathcal{E}^*_{\rm rad})$ is constant in time.

The Beltrami field can equally well be applied to the velocity field, i.e., $\boldsymbol{u}(x,t)=u_0\Theta(t)\,(0,\sin k_0x,\cos k_0x)^{\rm T}$. The normalized kinetic energy density is $\Omega_{\rm K}=\rho u_0^2/(2\mathcal{E}^*_{\rm rad})$. In this case, there would be no initial magnetic field, although it could be generated by a dynamo at later times, when $\eta\neq0$. Hence, this case would require solving the time-dependent MHD equations simultaneously with the GW equation, if $\eta=0$ cannot be assumed.

The fractional helicity of the Beltrami field is ±1 and has the same sign as the characteristic wavenumber k_0. The Beltrami field (when applied to $\boldsymbol{B}$) is force-free ($\boldsymbol{J}\times\boldsymbol{B}=\boldsymbol{0}$), so no velocity will be generated. In the absence of magnetic diffusion ($\eta=0$), we can therefore treat this magnetic field as given and do not need to evolve it. In the TT projection, we can write the normalized stress tensor as $T_{ij}^{\rm TT}(x,t)=(-B_iB_j+\frac{1}{2}\delta_{ij}\boldsymbol{B}^2)/\mathcal{E}^*_{\rm rad}$ for $i,j=2,3$ and $T_{ij}^{\rm TT}=0$ for $i=1$ and/or $j=1$. We have

$$T_{ij}^{\rm TT}(x,t) \;=\; -\,\Omega_{\rm M}\Theta(t)\begin{pmatrix}0&0&0\\ 0&-\cos2k_0x&\sin2k_0x\\ 0&\sin2k_0x&\cos2k_0x\end{pmatrix}. \tag{30}$$

Note that $T_{ij}^{\rm TT}(x,t)$ has only two independent terms, so we can directly compute the $+$ and $\times$ components. For the Beltrami magnetic field, we have

$$T_+(x,t) \;=\; \Omega_{\rm M}\Theta(t)\cos2k_0x, \qquad\qquad T_\times(x,t) \;=\; -\,\Omega_{\rm M}\Theta(t)\sin2k_0x\,. \tag{31}$$

These modes are directly obtained using the decomposition into the $+,\times$ polarization basis with the change of sign described in the footnote above. If the change of sign is not taken into account, the $\times$ mode obtained is $\tilde{T}_\times(x,t)\propto{\rm i}\cos2k_0x$, which is not independent of the $+$ mode. Since the $+$ and $\times$ modes have to be orthogonal functions, the change of sign is required to appropriately describe the modes.

Assuming $h_+=h_\times=\dot{h}_+=\dot{h}_\times=0$ at the initial time $t=0$, when the Beltrami field starts to act as a source of GWs, the time-dependent part of the solutions to the GW equation is proportional to

$1-\cos 2\omega_0 t = 2\sin^2\omega_0 t$, where $\omega_0 = ck_0$, so we have

$$h_+(x,t) \;=\; \frac{3H_*^2}{c^2k_0^2}\,\Omega_{\rm M}\Theta(t)\cos 2k_0x\,\sin^2\omega_0 t\,, \qquad\qquad h_\times(x,t) \;=\; -\,\frac{3H_*^2}{c^2k_0^2}\,\Omega_{\rm M}\Theta(t)\sin 2k_0x\,\sin^2\omega_0 t\,. \tag{32}$$

The spectral function S_h is given by

$$S_h(k,t) \;=\; \left(\frac{3H_*^2}{c^2k_0^2}\right)^2\Omega_{\rm M}^2\Theta(t)\delta(k-2\,k_0)\sin^4\omega_0 t\,, \tag{33}$$

where $\delta(k-2\,k_0)$ is the Dirac delta function, and the shell-integration is performed in 1D, such that we get a factor $\Omega_1 = 2$ in the computation. The characteristic wavenumber k_0 has been considered to be positive because the shell-integration rules out the dependence on direction of the wavevector $\boldsymbol{k}$, leading to a function that only depends on the positive modulus k. For negative k_0 the δ term should then be $\delta(k+2k_0)$ instead. In general, we write $\delta(k-2|k_0|)$. The $h_{\rm rms}(k,t)$ spectral function is

$$h_{\rm rms}(k,t) \;=\; \frac{3\sqrt{2}H_*^2}{c^2k_0^2}\sqrt{k_0}\Omega_{\rm M}\Theta(t)\delta(k-2\,|k_0|)\sin^2\omega_0 t\,, \tag{34}$$

which leads to a characteristic amplitude

$$h_{\rm rms}(t) \;=\; \left(\int_0^\infty S_h(k,t)\,{\rm d}k\right)^{1/2} \;=\; \frac{3H_*^2}{c^2k_0^2}\Omega_{\rm M}\Theta(t)\sin^2\omega_0 t\,. \tag{35}$$

The spectral function $S_{\dot h}(k,t)$ is given by

$$S_{\dot h}(k,t) \;=\; \left(\frac{3H_*^2}{ck_0}\right)^2\Omega_{\rm M}^2\Theta(t)\delta(k-2\,|k_0|)\sin^2 2\omega_0 t\,, \tag{36}$$

where we have used the time derivatives of the strains

$$\dot h_+(x,t) \;=\; \frac{3H_*^2}{ck_0}\Omega_{\rm M}\Theta(t)\cos 2k_0x\sin 2\omega_0 t, \qquad\qquad \dot h_\times(x,t) \;=\; \frac{3H_*^2}{ck_0}\Omega_{\rm M}\Theta(t)\sin 2k_0x\sin 2\omega_0 t\,. \tag{37}$$

4 Exponential evolution of the source in time

It is convenient to restrict our attention to the case of a purely monochromatic exponential growth of $\boldsymbol{B}$ at the rate γ_0. The magnetic energy increases then at the rate $2\gamma_0$. In the following, the notation simplifies when letting the argument t start at $t=0$, so that the actual time is simply $t+1$. Let us now assume that $\tilde T(\boldsymbol{k},t)$ is given by

$$\tilde T(\boldsymbol{k},t+1) = \theta(t)\,\tilde T_0(k)\,e^{2\gamma t}, \tag{38}$$

where $\theta(t)=1$ for $t>0$ and 0 otherwise is the Heaviside step function, and $\tilde T_0(k)$ is the Fourier transform of one of the two polarization modes of the stress, which is assumed to depend just on $k=|\boldsymbol{k}|$.

During the early growth phase, the expansion of the universe can be neglected and we can solve the GW equation in closed form as

$$\tilde h(k,t+1) = \frac{6\tilde T_0(k)}{k}\int_0^t \sin k(t-t')\,e^{2\gamma t'}\,{\rm d}t', \tag{39}$$

where $\tilde h$ stands for both $\tilde h_+$ and $\tilde h_\times$. Using $\sin\phi = (e^{{\rm i}\phi}-e^{-{\rm i}\phi})/2{\rm i}$ for any variable ϕ, we have

$$h = \frac{3T_0}{{\rm i}k}\int_0^t\left[e^{(2\gamma-{\rm i}k)t'+{\rm i}kt} - e^{(2\gamma+{\rm i}k)t'-{\rm i}kt}\right]{\rm d}t'. \tag{40}$$

Integrating between the two boundaries yields

$$h(k,t+1) = \frac{3T_0(k)}{\mathrm{i}k}\left[\frac{e^{2\gamma t}-e^{\mathrm{i}kt}}{2\gamma-\mathrm{i}k} - \frac{e^{2\gamma t}-e^{-\mathrm{i}kt}}{2\gamma+\mathrm{i}k}\right]. \tag{41}$$

Equation (41) can be written as

$$\tilde{h}(k,t+1) = \frac{6\tilde{T}_0(k)}{4\gamma^2+k^2}\left(e^{2\gamma t} - \cos kt - \frac{2\gamma}{k}\sin kt\right), \tag{42}$$

or, replacing $2\gamma \to k_0$,

$$\tilde{h}(k,t+1) = \frac{6\tilde{T}_0(k)}{k_0^2+k^2}\left(e^{k_0 t} - \cos kt - \frac{k_0}{k}\sin kt\right) \tag{43}$$

and its time derivative

$$k^{-1}\dot{\tilde{h}}(k,t+1) = \frac{6\tilde{T}_0(k)}{k_0^2+k^2}\left(\frac{k_0}{k}e^{k_0 t} + \sin kt - \frac{k_0}{k}\cos kt\right). \tag{44}$$

In practice, we are always interested in the case where the exponential term dominates over the cosine and sine terms. When $k < 2\gamma$, $\mathrm{Sp}(h)$ and $\mathrm{Sp}(\dot{h})$ are proportional to $\mathrm{Sp}(T_0)$. When the source has a white noise spectrum, we have $\mathrm{Sp}(h) \propto k^2[\tilde{T}_0(k)]^2 \propto k^2$. However, when $k > 2\gamma$, we find $\mathrm{Sp}(h) \propto \mathrm{Sp}(\dot{h}) \propto k^2[\tilde{T}_0(k)/k^2]^2 \propto k^{-2}$, with the breakpoint being at $ck = 2\gamma_0$, where we have restored the speed of light for dimensional clarity.

4.1 Solution for subsequent evolution

Let us assume that the souce is turned off abruptly at $t = t_0$. The GW field then continunues in a purely oscillatory fashion with

$$\begin{pmatrix} \tilde{h} \\ \dot{\tilde{h}}/k \end{pmatrix}(k,t+1) = \begin{pmatrix} \cos kt_\mathrm{m} & \sin kt_\mathrm{m} \\ -\sin kt_\mathrm{m} & \cos kt_\mathrm{m} \end{pmatrix}\begin{pmatrix} A \\ B \end{pmatrix}, \tag{45}$$

where the coefficients A and B have to be determined by matching $\tilde{h}$ and $\dot{\tilde{h}}$ of this solution to Equations (43) and (44) at $t = t_\mathrm{e}$, which we write as

$$\begin{pmatrix} \tilde{h}_\mathrm{m} \\ \dot{\tilde{h}}_\mathrm{m}/k \end{pmatrix} \equiv \frac{6\tilde{T}_0(k)}{k_0^2+k^2}\begin{pmatrix} e^{k_0 t_\mathrm{m}} - \cos kt_\mathrm{m} - \frac{k_0}{k}\sin kt_\mathrm{m} \\ \frac{k_0}{k}e^{k_0 t_\mathrm{m}} + \sin kt_\mathrm{m} - \frac{k_0}{k}\cos kt_\mathrm{m} \end{pmatrix}. \tag{46}$$

Thus, we require

$$\begin{pmatrix} \tilde{h}_\mathrm{m} \\ \dot{\tilde{h}}_\mathrm{m}/k \end{pmatrix} = \begin{pmatrix} \cos kt_\mathrm{m} & \sin kt_\mathrm{m} \\ -\sin kt_\mathrm{m} & \cos kt_\mathrm{m} \end{pmatrix}\begin{pmatrix} A \\ B \end{pmatrix}, \tag{47}$$

with the solution

$$\begin{pmatrix} A \\ B \end{pmatrix} = \begin{pmatrix} \cos kt_\mathrm{m} & \sin kt_\mathrm{m} \\ -\sin kt_\mathrm{m} & \cos kt_\mathrm{m} \end{pmatrix}\begin{pmatrix} \tilde{h}_\mathrm{m} \\ \dot{\tilde{h}}_\mathrm{m}/k \end{pmatrix} \tag{48}$$

Thus,

$$\begin{pmatrix} \tilde{h} \\ \dot{\tilde{h}}/k \end{pmatrix}(k,t+1) = \begin{pmatrix} \cos kt_\mathrm{m} & \sin kt_\mathrm{m} \\ -\sin kt_\mathrm{m} & \cos kt_\mathrm{m} \end{pmatrix}\begin{pmatrix} \cos kt_\mathrm{m} & \sin kt_\mathrm{m} \\ -\sin kt_\mathrm{m} & \cos kt_\mathrm{m} \end{pmatrix}\begin{pmatrix} \tilde{h}_\mathrm{m} \\ \dot{\tilde{h}}_\mathrm{m}/k \end{pmatrix} \tag{49}$$

or, using the addition theorems of trigonometric functions,

$$\begin{pmatrix} \tilde{h} \\ \dot{\tilde{h}}/k \end{pmatrix}(k,t+1) = \begin{pmatrix} \cos k(t-t_\mathrm{m}) & \sin k(t-t_\mathrm{m}) \\ -\sin k(t-t_\mathrm{m}) & \cos k(t-t_\mathrm{m}) \end{pmatrix}\begin{pmatrix} \tilde{h}_\mathrm{m} \\ \dot{\tilde{h}}_\mathrm{m}/k \end{pmatrix} \tag{50}$$

Table 1: Dependence of the numerical decay rate λ on $k_{\rm GW}/k_{\rm Ny}$ and $\delta t\,c/\delta x$.

$\delta t\,c/\delta x$	$k_{\rm GW}/k_{\rm Ny}=1/4$	$1/2$	1
0.2	6.7×10^{-4}	1.0×10^{-2}	6.0×10^{-2}
0.1	8.2×10^{-5}	1.3×10^{-3}	8.0×10^{-3}
0.05	1.2×10^{-5}	3.2×10^{-4}	1.0×10^{-3}

We thus have

$$\tilde{h}(k,t{+}1)=\frac{6\tilde{T}_0(k)}{k_0^2+k^2}\left[\cos k(t-t_{\rm m})\left(e^{k_0t_{\rm m}}-\cos kt_{\rm m}-\frac{k_0}{k}\sin kt_{\rm m}\right)+\sin k(t-t_{\rm m})\left(\frac{k_0}{k}e^{k_0t_{\rm m}}+\sin kt_{\rm m}-\frac{k_0}{k}\cos kt_{\rm m}\right)\right] \tag{51}$$

or

$$\tilde{h}(k,t{+}1)=\frac{6\tilde{T}_0(k)}{k_0^2+k^2}\left[\left(\cos k(t-t_{\rm m})+\frac{k_0}{k}\sin k(t-t_{\rm m})\right)\left(e^{k_0t_{\rm m}}-\cos kt_{\rm m}\right)-\left(\frac{k_0}{k}\cos k(t-t_{\rm m})+\sin k(t-t_{\rm m})\right)\sin kt_{\rm m}\right] \tag{52}$$

5 Numerical solutions for finite spatio-temporal resolution

At small enough grid spacings and small enough timesteps, our numerical solutions reproduce the considered one-dimensional Beltrami field. At coarser resolution, however, we find that $h_{\rm rms}(t)$ and $\Omega_{\rm GW}(t)$ are characterized by an additional decay of the form

$$h_{\rm rms}(t)\;=\;\left(3H_*^2/c^2k_0^2\right)\Omega_{\rm M}\,{\rm e}^{-\lambda t}\sin^2\omega_0 t\,, \tag{53}$$

$$\Omega_{\rm GW}(t)\;=\;\left(3H_*^2/2c^2k_0^2\right)\Omega_{\rm M}^2\,{\rm e}^{-\lambda t}\sin^2 2\omega_0 t\,, \tag{54}$$

where λ is the numerical decay rate. We emphasize that $\lambda\neq0$ is entirely artificial and has to do with imperfect numerics in the case of approach I. Results for λ are given in Table 1 as functions of δt (quantified by the Courant number $\delta t\,c/\delta x$) and the GW wavenumber $k_{\rm GW}$ (normalized by the Nyquist wavenumber $k_{\rm Ny}=\pi/\delta x$ to give $k_{\rm GW}/k_{\rm Ny}=k_{\rm GW}\delta x/\pi$).

The magnetic field wavenumber is $k_{\rm M}=k_0$, so $k_{\rm GW}=2k_0\;=2k_{\rm M}$ is the wavenumber of the GWs generated by the one-dimensional Beltrami field. We see from Table 1 that the decay rate is largest for $k_{\rm GW}=k_{\rm Ny}$ and varies there between 6×10^{-2} (for $\delta t\,c/\delta x=0.2$) and 10^{-3} (for $\delta t\,c/\delta x=0.05$). In Figure 2 we plot contours of λ (color-coded) versus $k_{\rm GW}$ and δt. Again, the largest values of λ occur when $k_{\rm GW}=k_{\rm Ny}$ and δt is large. We also see that the lines of constant decay rate scale like $\delta t\propto k_{\rm GW}^{-1}$. In Figure 3 we show, in separate panels, the changes in λ versus $k_{\rm GW}$ and δt. We see that the data points are compatible with the scalings $\lambda\propto k_{\rm GW}^3$ and $\lambda\propto\delta t^3$. The cubic scaling of λ is related to the third order accuracy of the time stepping scheme. The slight departures from this behavior can be attributed to the low number of runs computed to construct Table 1.

6 Exact solution between time steps for constant T

Consider the GW equation, $\ddot{h}+k^2h=S$, in the form

$$\begin{aligned}\dot{h}&=g\\ \ddot{h}\equiv\dot{g}&=-k^2h+S.\end{aligned} \tag{55}$$

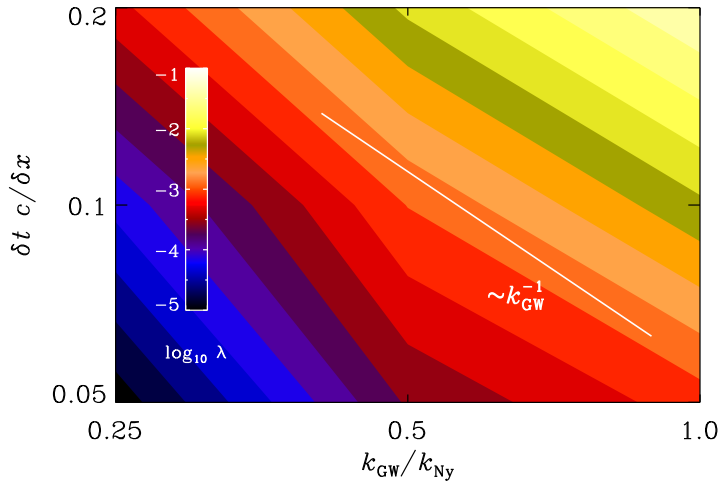

Figure 2: Dependence of the decay rate of the Beltrami field solution due to numerical error, λ, on $k_{\rm GW}/k_{\rm Ny}$ and $\delta t\, c/\delta x$. Blue (yellow) shades indicate low (high) numerical errors. The error is high when $k_{\rm GW}$ is close to the Nyquist wavenumber and δt is large. The scaling $\delta t\, c/\delta x \propto (k_{\rm GW}/k_{\rm Ny})^{-1}$ is indicated by a white solid line.

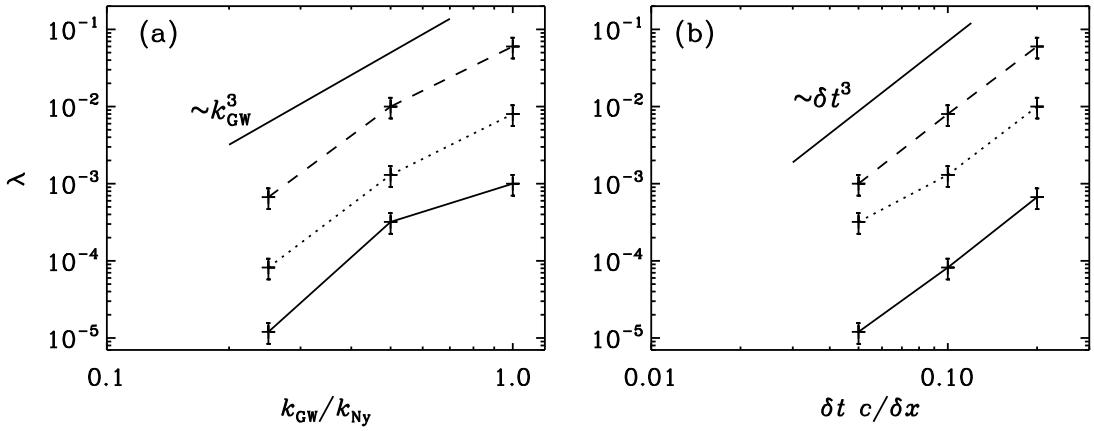

Figure 3: Scaling of the decay rate of the Beltrami field solution due to numerical error, λ, with $k_{\rm GW}/k_{\rm Ny}$ (left panel) for $\delta t\, c/\delta x = 0.05$ (straight line), 0.1 (dotted line), and 0.2 (dashed line), and with $\delta t\, c/\delta x$ (right panel) for $k_{\rm GW}/k_{\rm Ny} = 0.25$ (straight line), 0.5 (dotted line), and 1.0 (dashed line). Cubic scalings are indicated by the straight lines.

Suppose we know h, g, and S at time $t = 0$, what is the solution at time $t = \delta t$ under the assumption that $S = $ const during the time interval δt. The general solution can be written in the form

$$\begin{aligned} h &= +A\cos kt + B\sin kt + k^{-2}S \\ g &= -Ak\sin kt + Bk\cos kt, \end{aligned} \tag{56}$$

where A and B are unknowns that are determined from the solution (h, g) at $t = 0$, which leads to

$$\begin{aligned} A &= h - k^{-2}S \\ B &= k^{-1}g \end{aligned} \tag{57}$$

Inserting this yields for the solution at $t = \delta t$

$$\begin{aligned} h(\delta t) &= +(h - k^{-2}S)\cos k\delta t + k^{-1}g \sin k\delta t + k^{-2}S, \\ g(\delta t) &= -(h - k^{-2}S)k \sin k\delta t + k^{-1}gk \cos k\delta t, \end{aligned} \tag{58}$$

or

$$\begin{aligned} h(\delta t) - k^{-2}S &= +(h - k^{-2}S)\cos k\delta t + k^{-1}g \sin k\delta t, \\ g(\delta t) &= -(h - k^{-2}S)k \sin k\delta t + k^{-1}gk \cos k\delta t, \end{aligned} \tag{59}$$

It is convenient to cancel a k factor in the last equation and to multiply the first equation by k, so

$$\begin{aligned} (kh - k^{-1}S)(\delta t) &= +(kh - k^{-1}S)\cos k\delta t + g \sin k\delta t, \\ g(\delta t) &= -(kh - k^{-1}S)\sin k\delta t + g \cos k\delta t. \end{aligned} \tag{60}$$

Writing this in matrix form yields

$$\begin{pmatrix} kh - k^{-1}S \\ g \end{pmatrix}_{\rm new} = \begin{pmatrix} \cos k\delta t & \sin k\delta t \\ -\sin k\delta t & \cos k\delta t \end{pmatrix} \begin{pmatrix} kh - k^{-1}S \\ g \end{pmatrix}_{\rm current} \tag{61}$$

for the solution at the next time. This technique was first exploited by Roper Pol et al. (2020).

7 Linearly varying S between time steps

When S varies linearly in time, the general solution can be written in the form

$$\begin{aligned} h &= +A\cos kt + B\sin kt + k^{-2}(S_0 + \dot{S}_0 \delta t) \\ g &= -Ak\sin kt + Bk\cos kt + k^{-2}\,\dot{S}_0 \end{aligned} \tag{62}$$

We can then express

$$\begin{pmatrix} kh - k^{-1}(S_0 + \delta S) \\ g - k^{-2}\delta S/\delta t \end{pmatrix}_{\rm new} = \begin{pmatrix} \cos k\delta t & \sin k\delta t \\ -\sin k\delta t & \cos k\delta t \end{pmatrix} \begin{pmatrix} kh - k^{-1}S \\ g - k^{-2}\delta S/\delta t \end{pmatrix}_{\rm current} \tag{63}$$

Comparing with the previous solution for constant source, we have

$$\begin{pmatrix} h \\ g \end{pmatrix}_{\rm 2nd\ order} = ... + \frac{\delta S}{k^2} \begin{pmatrix} [1 - (\sin k\delta t)/k\delta t] \\ (1 - \cos k\delta t)/\delta t \end{pmatrix}. \tag{64}$$

8 Timestep constraint for approach I in a turbulent case

We now present an example where the timestep constraint becomes particularly apparent when directly integrating the GW equation. As alluded to in the introduction, this is the case when GWs are being sourced by turbulent stresses, and we use the approach I. We consider here the case of decaying helical magnetic turbulence. This case was originally considered in the cosmological context using just an irregular magnetic field and no flow as the initial condition (**???**). In this context, one can argue that the magnetic field at scales larger than the injection scale must be causally related. This, together with the solenoidality of the magnetic field, leads to a k^4 subinertial range spectrum (**?**). The $E_{\rm M}(k,t) \propto k^4$ scaling corresponds to $\Omega_{\rm M}(k,t) \propto k^5$. The magnetic field is strong and the fluid motions are just the result of the Lorentz force. The k^4 subinertial range spectrum is then followed by a k^{-2} weak turbulence spectrum at high wavenumbers (Brandenburg et al., 2015). The normalized wavenumber where the change of behavior occurs, is the peak wavenumber, k_*. For an initial k^4 spectrum, the magnetic field undergoes inverse cascading such that the magnetic energy spectrum is self-similar and obeys

$$\Omega_{\rm M}(k,t)/k \;=\; \phi\,(k\xi_{\rm M}(t))\,, \tag{65}$$

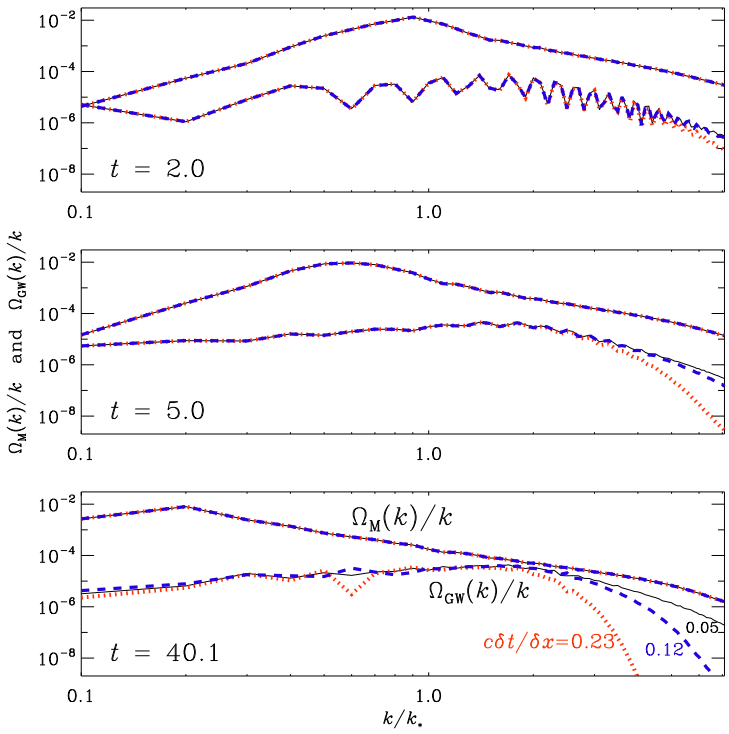

Figure 4: GW (lower curves) and magnetic (upper curves) energy spectra at three different normalized conformal times, $t = 2$ (top panel), 5 (middle panel), and 40 (bottom panel), which are normalized with the time when the turbulence source turns on, i.e., t_*. Each panel shows three different Courant numbers: $\delta t\, c/\delta x = 0.23$ (red dotted lines), 0.12 (blue dashed lines), and 0.05 (black solid lines). The wavenumbers are normalized with the normalized peak wavenumber k_*, at the starting time of generation. In this simulation, $k_* = 10$, and the total initial magnetic field energy density is $\Omega_{\rm M}\,(t = 1) \approx 0.123$.

where ϕ is a generic function (**??**) and $\xi_{\rm M}(t)$ is the magnetic integral scale given by (**??**).

In Figure 4 we show, for three different times, the normalized magnetic and GW energy spectra, obtained following approach I, for an expanding universe, so we have $\mathcal{G}(t) = 6/t$ on the right-hand side of (**??**), and $t = 1$ is the initial normalized time, which refers to the starting time of generation. Independent of the value of δt, the peak of $\Omega_{\rm M}(k,t)/k$ is seen to propagate gradually towards smaller k. This is the inverse cascade owing to the presence of magnetic helicity (**???**). Note that the peak of the spectrum always has the same height. This is compatible with (65). The ratio of $\Omega_{\rm M}(t)/\Omega_{\rm GW}(t)$ changes from about 100 at early times to about 20 at the last time as the magnetic field decays, while $\Omega_{\rm GW}(t)$ stays approximately constant.

Let us now focus on the comparison of solutions for different Courant numbers, $\delta t\, c/\delta x = 0.23$, 0.12, and 0.05 in Figure 4. While the magnetic energy spectra are virtually identical for different δt, even for high wavenumbers, the GW spectra are not. There is a dramatic loss of power at large k, when $\delta t\, c/\delta x = 0.23$. A value of $\delta t\, c/\delta x = 0.8$ was always found to be safe as far as the hydrodynamics is concerned, but this is obviously not small enough for the GW solution. This is a surprising result that may not have been noted previously.

In Figure 5, we show that the solution with $\delta t\, c/\delta x \lesssim 0.05$ agrees perfectly with that of approach II at $\delta t\, c/\delta x \lesssim 0.8$. The additional cost in performing Fourier transforms at every timestep, used in approach II, is easily outweighed by the more than 10 times longer timestep, when comparing to approach I. We also show the comparison between the actual GW energy spectrum, $\Omega_{\rm GW}(k,t)$; see (**??**), and the spectrum obtained from conformal time derivatives, $\Omega^{h'}_{\rm GW}(k,t)$; see (**??**). These two spectra become more similar

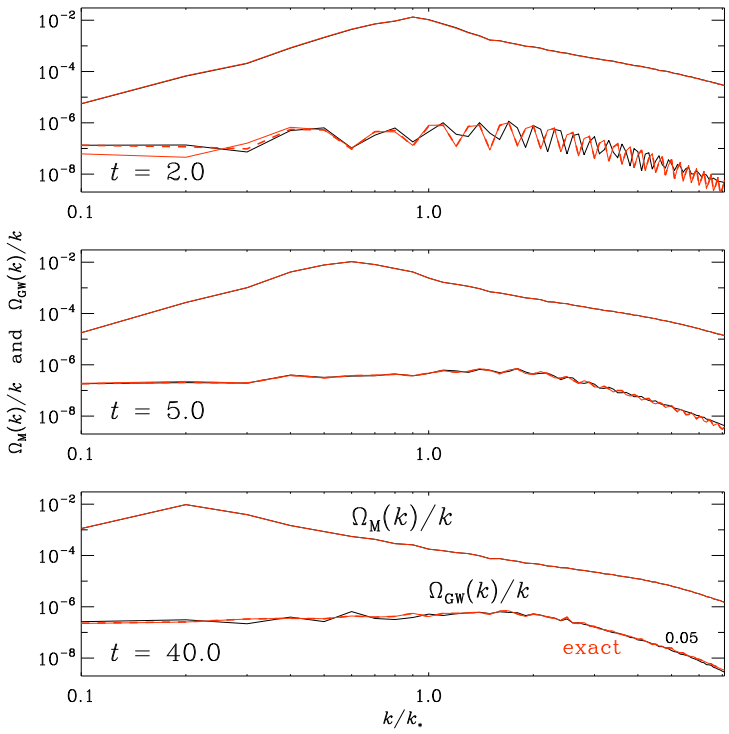

Figure 5: Same as Figure 4, but now comparing the case with $\delta t\, c/\delta x = 0.05$ (black solid lines), using approach I, with the analytic solution assuming constant $\mathcal{G}(t)T_{ij}(\boldsymbol{x},t)$, in time, between consecutive timesteps (red solid line), which corresponds to approach II, here referred to as "exact", using $\delta t\, c/\delta x = 0.8$. The red dashed lines indicate the spectrum computed from the conformal time derivatives of the strains, $\Omega^{\rm h'}_{\rm GW}(k,t)/k$.

Table 2: Dependence of the decay rate of the numerical error λ on $k_{\rm GW}/k_{\rm Ny}$ and $\delta t\, c/\delta x$ for hydromagnetically driven GWs. Dashes indicate that the decay rate was too small compared with the fluctuations and could not be determined.

$\delta t\, c/\delta x$	$k_{\rm GW}/k_{\rm Ny} = 1/4$	1/2	1
0.23	0.012	0.16	1.1
0.12	–	0.015	0.12
0.05	–	–	0.006

for large wavenumbers and for longer times.

To see whether the observed degradation using approach I; see Figure 4, is compatible with what has been seen for the monochromatic Beltrami field, we determine again the decay rates for three wavenumbers of the spectral GW amplitude. The result is given in Table 2.

In addition to the numerical error discussed above, when computing the solution using approach I, we found a numerical instability that is distinct from the usual one invoked in connection with the CFL condition. This new instability emerges when the accuracy of the solution is already strongly affected by the length of the timestep, namely for $\delta t\, c/\delta x \gtrsim 0.46$, which is still well within the range of what would normally (in hydrodynamics) be numerically stable. The problem appears at late times, after the GW spectrum has long been established. This new numerical error manifests itself as an exponential

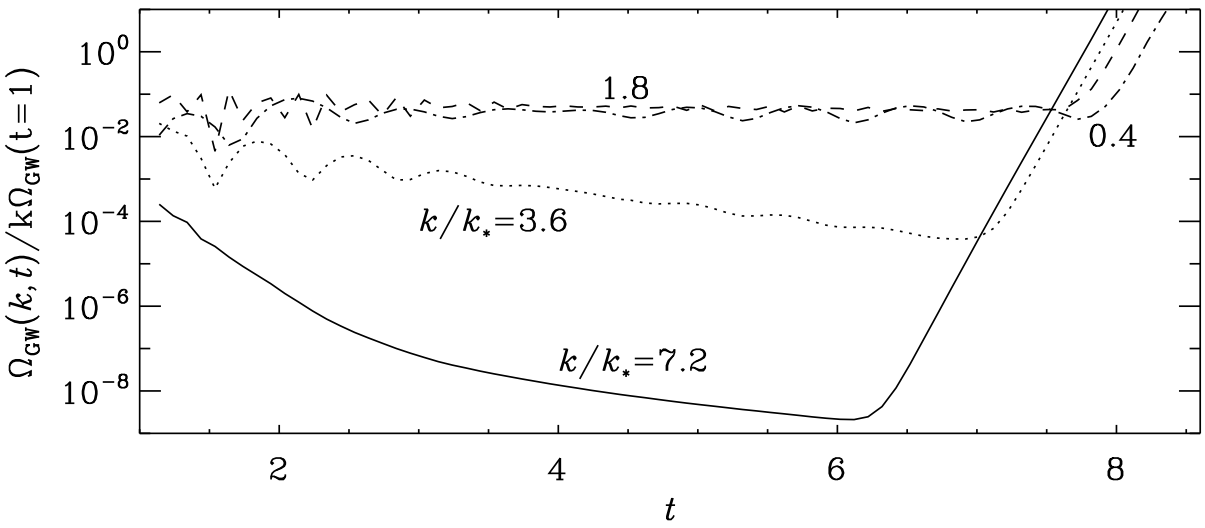

Figure 6: Late time numerical instability for $\delta t\, c/\delta x = 0.46$ seen in the temporal evolution of $\Omega_{\rm GW}(k,t)/k$ after $t = 6$ for $k/k_* = 7.2$ (solid), 3.6 (dotted), 1.8 (dashed), and 0.4 (dash-dotted). The spectra shown are normalized with the total GW energy density shortly after the start of the simulation, at $t \gtrsim 1$, $\Omega_{\rm GW}(k,t)/k\Omega_{\rm GW}(t \gtrsim 1)$. The normalized peak wavenumber is $k_* = 10$, and the total initial magnetic energy density is $\Omega_{\rm M}\,(t = 1) \approx 0.123$.

growth that is seen first at large wavenumbers and then at progressively smaller ones; see Figure 6. Our earlier studies have shown that this problem cannot be controlled by adding explicit diffusion to the GW equation. Given that the solution is already no longer accurate for this length of the timestep, this numerical instability was not worth further investigation, but it highlights once again the surprising differences in the numerical behavior of wave and fluid equations.

Looking again at the GW energy spectra at early times, Figures 4 and 5, we see wiggles in the spectrum at $t = 2$ (top panel). One might be concerned that these are caused by numerical artifacts, but the spatial distributions of physical $h_+(\boldsymbol{x}, t = 2)$ and $h_\times(\boldsymbol{x}, t = 2)$ look smooth; see Figure 7. Thus, the wiggles in $\Omega_{\rm GW}(k,t)/k$ are not artificial, but presumably related to the finite domain size and the way the initial condition for the magnetic field, $\Omega_{\rm M}\,(k, t = 1)/k$ is posed using combined k^4 and k^{-2} power laws, for small and large wavenumbers respectively. They might appear as a transient effect in the evolution from the initially vanishing GW energy density to the shape observed for later times. Indeed, at late times the wiggles disappear.

9 Can the timestep cause artifacts in hydrodynamic and MHD turbulence?

The length of the timestep can affect the convergence properties of solutions of incompressible hydrodynamic simulations. In the present compressible MHD simulations, however, no obvious side effects of increasing the length of the timestep within the standard CFL condition have been seen. However, there could be subtle effects. Here we investigate two possibilities. The first is the bottleneck effect in hydrodynamic turbulence, which refers to the kinetic energy spectrum, $\Omega_{\rm K}(k,t)/k$, slightly shallower than the Kolmogorov $k^{-5/3}$ spectrum. This phenomenon is explained by the inability of triad interactions with modes in the dissipative subrange to dispose of turbulent energy from the end of the inertial range (**?**). This also has subtle effects on the growth rate of turbulent small-scale dynamos (see Brandenburg et al.,

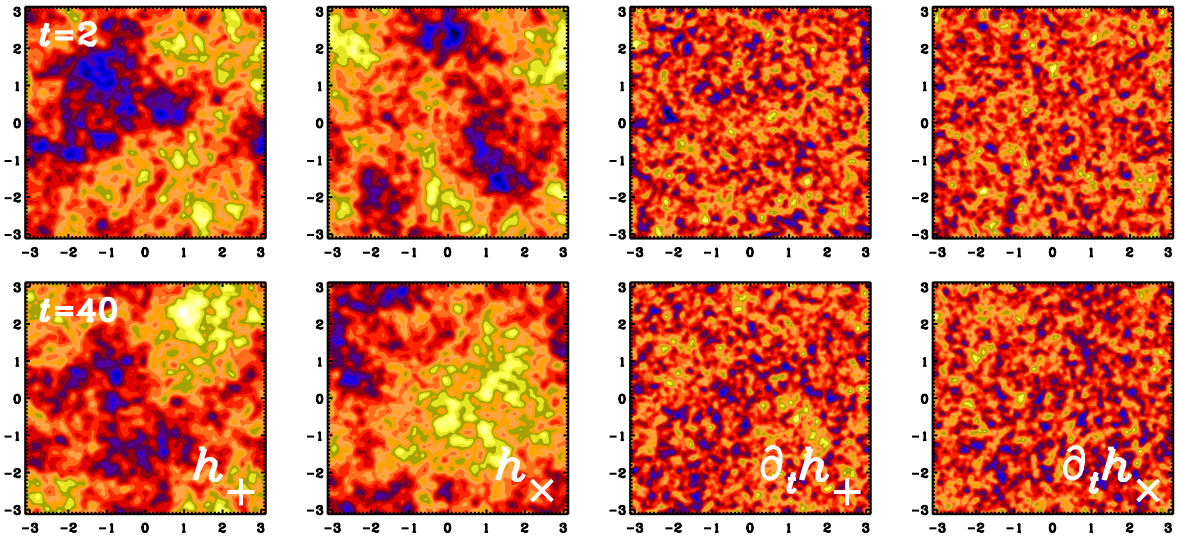

Figure 7: xy cross-sections through $z = 0$ of $h_+(\boldsymbol{x},t)$, $h_\times(\boldsymbol{x},t)$, and the normalized conformal time derivatives, $h'_+(\boldsymbol{x},t) = \partial_t h_+(\boldsymbol{x},t)$, and $h'_\times(\boldsymbol{x},t) = \partial_t h_+(\boldsymbol{x},t)$, at $t = 2$ (upper row) and $t = 40$ (lower row). The simulation parameters are the same as in Figures 4 and 5.

2018, hereafter referred to as BHLS). The second possible subtlety is a modification of the magnetic energy spectrum, $\Omega_{\rm M}(k,t)/k$, during the kinematic growth phase. This problem of a kinematic small-scale dynamo is closest to our GW experiment in that both problems are linear and there is no turbulent cascade in either of the two problems. We begin with the first possibility.

The description in this section refers only to MHD turbulence and, for convenience, the usual non-normalized and physical variables are used for comparison with other works (e.g., k refers to dimensional physical wavenumbers), instead of the normalized variables that are useful in the context of GWs. As in previous sections, however, we continue to show magnetic and kinetic energy spectra in terms of $\Omega_{\rm M,K}(k,t)/k$.

In the simulations of BHLS, turbulence was being forced at low wavenumbers using an explicit forcing function $\boldsymbol{f}(\boldsymbol{x},t)$ on the momentum equation. It drives modes in a narrow band of wavenumbers. We consider here run D of BHLS, where driving was applied at wavenumbers between 1.4 and 1.8 times the lowest wavenumber of the domain, $k_{\rm min} = 2\pi/L$ of a cubic domain of size L^3. The magnetic Reynolds number based on the average wavenumber was about 540.

The important point of BHLS was to show that the bottleneck effect is independent of the forcing wavenumber, provided that the effective forcing wavenumber is used in the definition of the magnetic Reynolds number. Here we demonstrate that the bottleneck is not affected by the length of the timestep. Technically, the simulations presented in this section are done with magnetic fields included, but the field is at all scales still extremely weak, so for all practical purposes we can consider those as hydrodynamic simulations. The result is shown in Figure 8, where we compare run D of BHLS, which uses a timestep of $\delta t\, c_{\rm s}/\delta x = 0.6$, with a new one called run Ds, where 's' indicates that the timestep is shorter, such that now $\delta t\, c_{\rm s}/\delta x = 0.15$, where $c_{\rm s}$ refers to the sound speed. Both spectra fall off in the same way as k approaches the viscous cutoff wavenumber $k_\nu = (\epsilon_{\rm K}/\nu^3)^{1/4}$, where $\epsilon_{\rm K}$ is the mean kinetic energy injection rate per unit mass, and ν is the kinematic viscosity.

It turns out that there is no difference in the energy spectrum relative to run D, where the timestep obeys $\delta t\, c_{\rm s}/\delta x = 0.60$. Thus, the artifacts reported in the present paper, namely the excessive damping of power at high wavenumbers, seem to be confined to the GW spectrum and do not affect in any obvious way the properties of the energy spectrum of MHD turbulence.

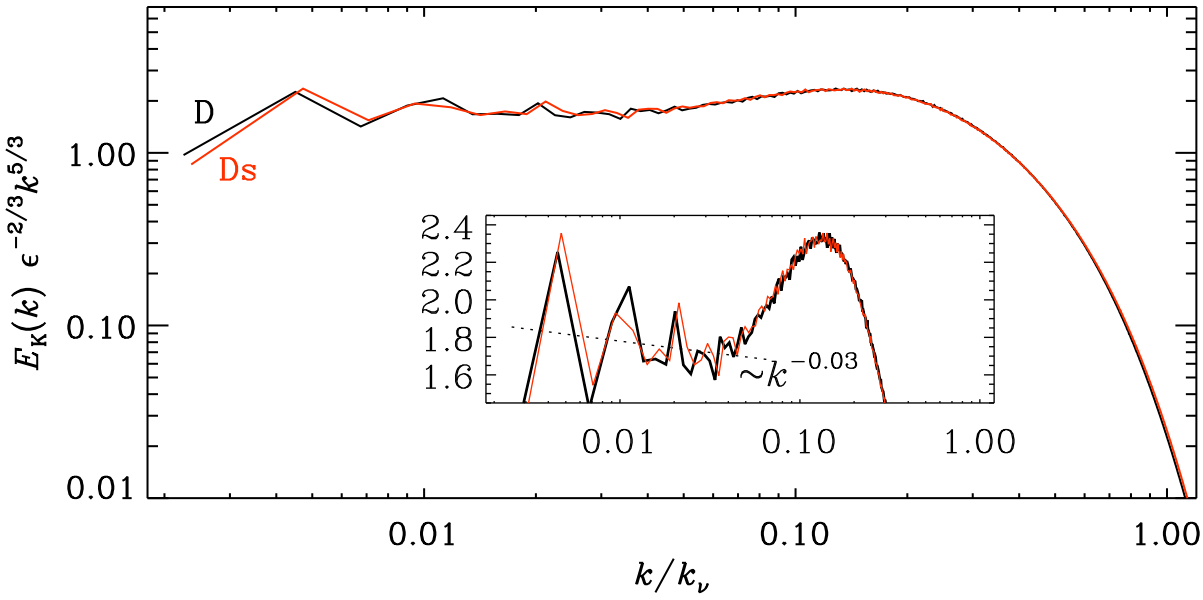

Figure 8: Comparison of the kinetic spectrum compensated with the usual Kolmogorov inertial scaling $k^{-5/3}\epsilon_{\rm K}^{2/3}$, for run D (black line) of BHLS with those of a continuation of this run with a four times shorter timestep (run Ds, red line). The inset shows the compensated spectra on a linear scale. The dotted line shows the expected inertial range correction proportional to $k^{-0.03}$. The physical wavenumbers are normalized with the dissipation wavenumber k_ν. Both spectra are time-averaged after compensating against the exponential growth.

The lack of any noticeable high wavenumber artifacts in MHD turbulence can simply be explained by the absence of relatively rapid oscillations in MHD flows, compared to GW oscillations, which are proportional to c. To demonstrate this, we compare in Figure 9 the GW frequency $\omega = ck$ with the turbulent turnover rate $u_k(k)k$, the turbulent Alfvén rate $v_{{\rm A}k}(k)k$, and the viscous damping rate νk^2 at wavenumber k for a simulation of GWs at 1152^3 mesh points, a Reynolds number, ${\rm Re} = u_{\rm rms}/\nu k$ of about 1000, and a magnetic Reynolds number ${\rm Rm} = {\rm Re}$, so that $\nu = \eta$. Here, we use the relations $u_k(k) = \sqrt{2E_{\rm K}(k)}$, and $v_{{\rm A}k}(k) = \sqrt{2E_{\rm M}(k)}$ for the k-dependent turbulent velocity and the k-dependent Alfvén speed. Note that $\max(v_{{\rm A}k}(k)\,k)$, at $ck/H_* \approx 3\cdot10^{-4}$, is about 30 times smaller than $\omega = ck$, and the difference is bigger for larger values of k. This shows that from an accuracy point of view, the timestep could well be 30 times longer before the accuracy of MHD begins to be affected.

10 Present day values of GW energy and characteristic strain

We recall that the dots in the GW equation denote physical time derivatives. In terms of the normalized conformal time t and scaled strains $h_{ij}(\boldsymbol{x},t)$, the physical time derivative of the physical strains $h_{ij}^{\rm phys}(\boldsymbol{x},t)$ is

$$\dot{h}_{ij}^{\rm phys}(\boldsymbol{x},t) \;=\; \frac{H_*}{t}\frac{\partial}{\partial t}\left(\frac{h_{ij}(\boldsymbol{x},t)}{t}\right) \;=\; \frac{H_*}{t^2}\left(h'_{ij}(\boldsymbol{x},t) - \frac{h_{ij}(\boldsymbol{x},t)}{t}\right). \tag{66}$$

Therefore, the normalized GW energy density $\Omega_{\rm GW}^0(t)$ can be expressed in terms of the normalized conformal time as

$$\Omega_{\rm GW}^0(t) \;=\; \frac{(H_*/H_0)^2}{12t^4}\left[\langle h'_{ij}h'_{ij}\rangle + \frac{1}{t^2}\langle h_{ij}h_{ij}\rangle - \frac{2}{t}\langle h'_{ij}h_{ij}\rangle\right], \tag{67}$$

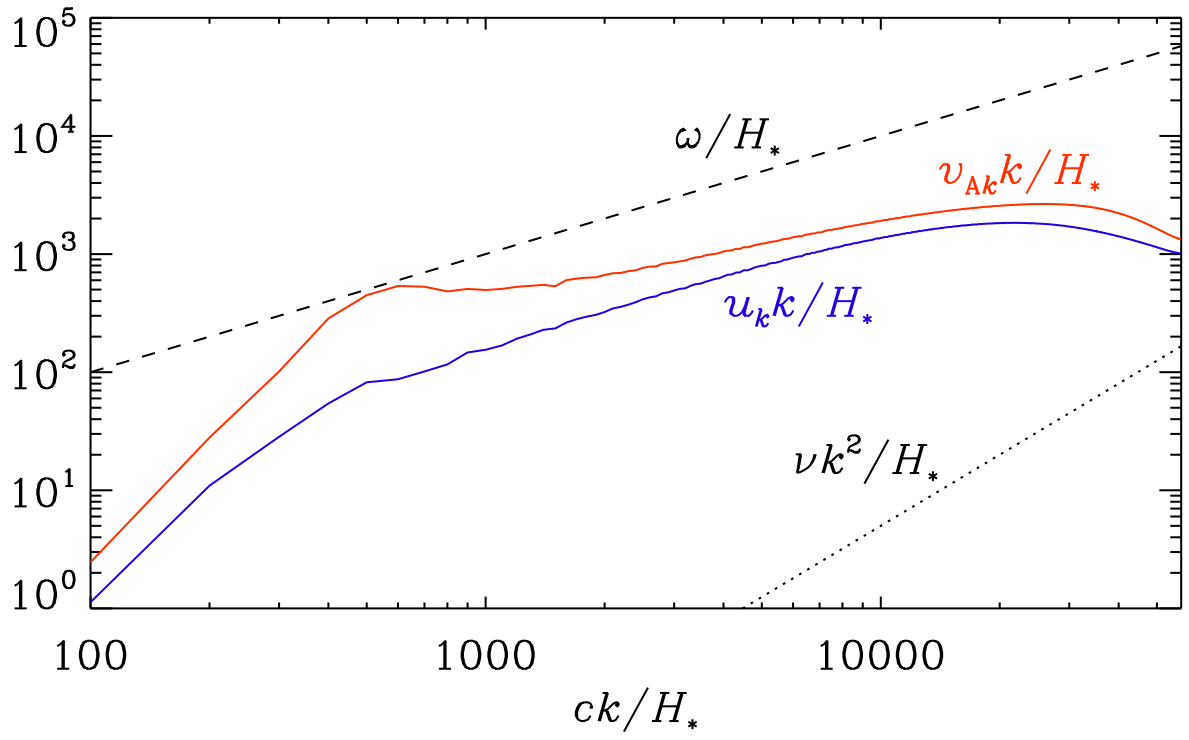

Figure 9: Comparison of the GW frequency $\omega = ck$ with the turnover rate $u_k(k)\,k$ of the turbulence, the turbulent Alfvén rate $v_{\mathrm{A}k}(k)\,k$, and the viscous damping rate νk^2 at normalized wavenumber ck/H_*. Note that all frequencies in the plot are normalized with H_*.

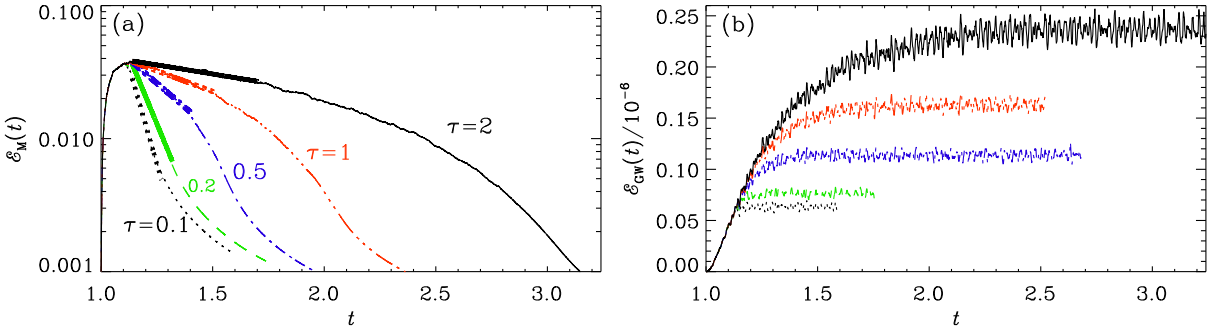

Figure 10: Evolution of magnetic energy (a) and growth of GW energy density (b) for simulations where the driving is turned off at $t = 1.1$ (black dotted line), or the strength of the driving is reduced linearly in time over the duration $\tau = 0.2$ (green), 0.5 (blue), 1 (red), or 2 (black). Time is in units of the Hubble time at the moment of source activation. The magnetic and GW energy densities are in units of the radiation energy density. In (a), the fat line segments denote a decay proportional to $\exp(\lambda t)$ with λ given in Table 3.

where the explicit dependence on $\boldsymbol{x}$ and t has been omitted to simplify the notation. The energy density $\Omega^0_{\rm GW}(t)$ has three different contributions such that $\Omega^0_{\rm GW}(t) = \Omega^{\rm h',0}_{\rm GW}(t) + t^{-2}\Omega^{\rm h,0}_{\rm GW}(t) - 2t^{-1}\Omega^{\rm mix,0}_{\rm GW}(t)$. Note that $\Omega_{\rm GW}(t)$ is obtained from (67) without the prefactor H_*/H_0, as well as $\Omega^i_{\rm GW}(t)$, for $i = {\rm h}'$, h, mix.

As an example, we show the temporal evolution of the GWs. The GW spectrum becomes stationary shortly after the driving of the source ends (i.e., when the free decay stage of the source starts), while the energy density of the source is still present. To demonstrate this, Kahniashvili et al. (2021) drive magnetic fields with an electromotive force, $\mathcal{F}_i = (\delta_{ij} + \sigma\epsilon_{ijl}\hat{k}_l)\mathcal{F}^{(0)}_j$, consisting of plane waves that are delta-correlated in time. Here, $-1 \leq \sigma \leq 1$ quantifies the fractional helicity, and $\mathcal{F}^{(0)}_j$ is a nonhelical plane-wave forcing term. Plasma motions are selfconsistently driven by the Lorentz force. Purely hydrodynamic motions are driven by a ponderomotive force analogous to $\mathcal{F}_i$.

In Fig. 10, we show the temporal evolution of the source and the growth of the GW energy density for the driven ($1 < t < 1.1$) and decaying stages ($t > 1.1$), where the driving decreases linearly for a duration $\tau = 0.1$–2, although $\tau > 0.5$ may be unrealistic. As in Roper Pol et al. (2020), they use 1152^3 meshpoints for the runs in Fig. 10 and put $\sigma = 0$; see Table 3 for a summary relevant quantities. During the statistically stationary stage, the GW energy density growth rate is proportional to the duration of turbulence. In reality, the driving stage is short compared to the Hubble time-scale, and consists of the few largest eddy turnover times.

Table 3: Characteristic parameters of the runs of Fig. 10.

τ	λ	$\mathcal{E}^{\rm max}_{\rm M}$	$\mathcal{E}^{\rm max}_{\rm K}$	$\mathcal{E}^{\rm sat}_{\rm GW}$	$h^{\rm sat}_{\rm rms}$
0.1	-13.5	0.0367	0.0134	6.3×10^{-8}	2.5×10^{-6}
0.2	-9.37	0.0368	0.0135	7.6×10^{-8}	2.8×10^{-6}
0.5	-3.32	0.0372	0.0137	1.1×10^{-7}	3.4×10^{-6}
1	-1.43	0.0378	0.0140	1.6×10^{-7}	4.1×10^{-6}
2	-0.63	0.0381	0.0141	2.4×10^{-7}	5.1×10^{-6}

In Table 3, we have quoted the values of $\mathcal{E}^{\rm sat}_{\rm GW}$ and $h^{\rm sat}_{\rm rms}$ obtained at the end of the simulation at $t = t_{\rm end}$. We emphasize that $\mathcal{E}_{\rm GW}$ is the comoving GW energy density normalized by the critical energy density, which is the same as the radiation energy density during the simulation, and $h_{\rm rms}$ corresponds to the scaled strain. To compute the relic observable $h_0^2\Omega_{\rm GW}$ at the present time, we have to multiply

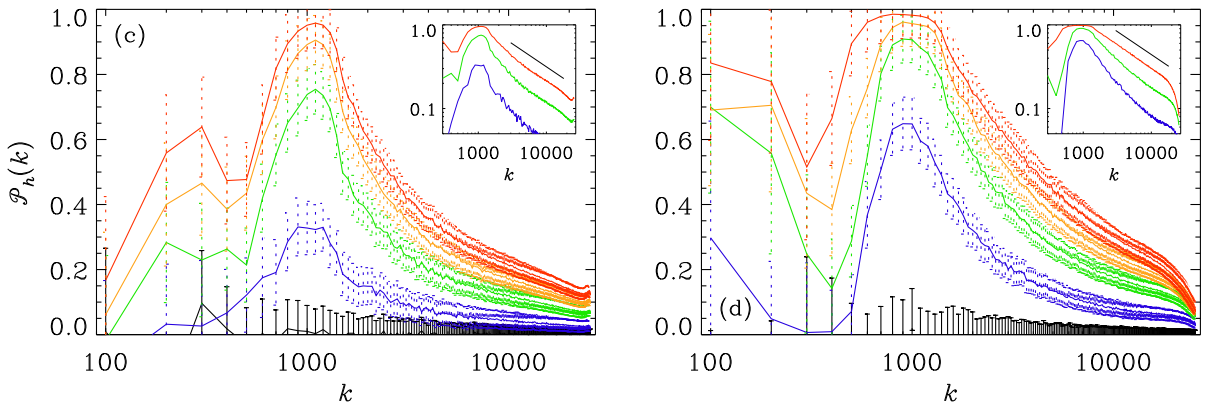

Figure 11: Degree of circular polarization for (a) kinetically and (b) magnetically forced cases with $\sigma = 0$ (black) 0.1 (blue), 0.3 (green), 0.5 (orange), and 1 (red). Approximate error bars based on the temporal fluctuations and statistical spread for different random seeds of the forcing are shown as solid black lines for $\sigma = 0$ and as dotted lines otherwise. The wave number is in units of the comoving Hubble frequency.

$\mathcal{E}_{\rm GW}^{\rm sat}$ by a factor $(H_*/H_0)^2 a_0^{-4}$. although there we used the symbol $\Omega_{\rm GW}$ also for the latter. For the aforementioned fiducial parameters of $g_* = 100$ and $T_* = 100\,{\rm GeV}$, this factor is 1.64×10^{-5}. The largest value of $\mathcal{E}_{\rm GW}^{\rm sat}$ quoted in Table 3 is 2.4×10^{-7} and corresponds therefore to $h_0^2 \Omega_{\rm GW} = 4 \times 10^{-12}$. Likewise, the values of $h_{\rm rms}^{\rm sat}$ in Table 3 have to be multiplied by $a_0^{-1} = 8.0 \times 10^{-16}$ to obtain the observable h_c at the present time. Again, the largest value of $h_{\rm rms}^{\rm sat} = 5.1 \times 10^{-6}$ corresponds therefore to the observable $h_c = 4 \times 10^{-21}$.

11 Helical turbulence

Figure 11 shows polarization degree spectra in for continuous pumping of kinetic or magnetic energy and helicity at intermediate scales. These results demonstrate that the polarization degree is scale-dependent: $\propto k^{-0.5}$ at large wavenumbers, which is shallower than the k^{-1} expected for Kolmogorov-like helical turbulence with different spectral indices for the magnetic spectral energy density ($n_S = -5/3$) and the spectral helicity density ($n_H = -11/3$). In these simulations, the actual indices are a bit smaller, which also explains the shallower slope in the polarization degree.

12 GW from the QCD epoch

In Figure 12, we plot the resulting present-day GW energy and strain spectra for runs with $k_{\rm f} = 2$, 6, 20, and 60 with helicity in the driving function $\boldsymbol{\mathcal{F}}$ see Brandenburg et al. (2021). The first two cases with $k_{\rm f} = 2$ and 6 lie well within the frequency and amplitude range accessible to NANOGrav. In all cases, the spectra show a sharp drop slightly above the peak frequency. This is a consequence of the rapid temporal growth of the spectra, which leads to a correspondingly large growth at the peak frequency, while at higher frequencies, the spectrum settled at values that were determined by somewhat earlier times when the energy was still weaker. Better agreement was obtained in the work by Roper Pol et al. (2022).

References

Brandenburg, A., Kahniashvili, T., & Tevzadze, A. G., "Nonhelical inverse transfer of a decaying turbulent magnetic field," *Phys. Rev. Lett.* **114**, 075001 (2015).

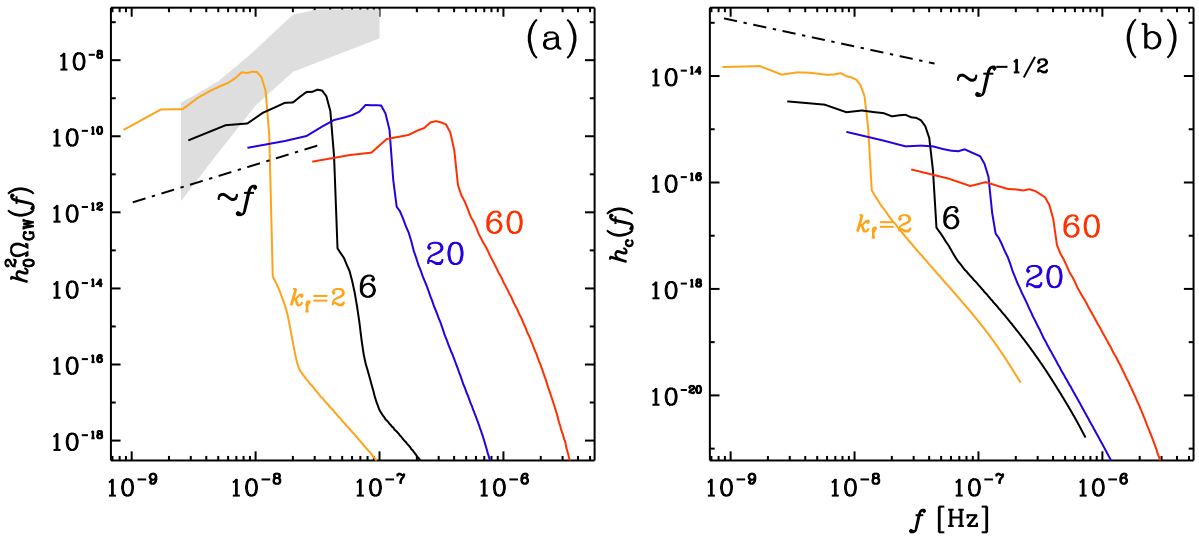

Figure 12: (a) $h_0^2\Omega_{\rm GW}(f)$ and (b) $h_c(f)$ at the present time for helical runs. The 2σ confidence contour for the 30-frequency power law of the NANOGrav 12.5-year data set is shown in gray. Adapted from Brandenburg et al. (2021)

Brandenburg, A., Clarke, E., He, Y., & Kahniashvili, T., "Can we observe the QCD phase transition-generated gravitational waves through pulsar timing arrays?" *Phys. Rev. D* **104**, 043513 (2021).

Brandenburg, A., He, Y., Kahniashvili, T., Rheinhardt, M., & Schober, J., "Gravitational waves from the chiral magnetic effect," *Astrophys. J.* **911**, 110 (2021).

Brandenburg, A., Haugen, N. E. L., Li, X.-Y., & Subramanian, K., "Varying the forcing scale in low Prandtl number dynamos," *Month. Not. Roy. Astron. Soc.* **479**, 2827–2833 (2018).

Kahniashvili, T., Brandenburg, A., Gogoberidze, G., Mandal, S., & Roper Pol, A., "Circular polarization of gravitational waves from early-universe helical turbulence," *Phys. Rev. Res.* **3**, 013193 (2021).

Roper Pol, A., Mandal, S., Brandenburg, A., Kahniashvili, T., & Kosowsky, A., "Numerical simulations of gravitational waves from early-universe turbulence," *Phys. Rev. D* **102**, 083512 (2020).

Roper Pol, A., Brandenburg, A., Kahniashvili, T., Kosowsky, A., & Mandal, S., "The timestep constraint in solving the gravitational wave equations sourced by hydromagnetic turbulence," *Geophys. Astrophys. Fluid Dynam.* **114**, 130–161 (2020).

Roper Pol, A., Caprini, C., Neronov, A., & Semikoz, D., "
," *Phys. Rev. D* **105**, 123502–Gravitational wave signal from primordial magnetic fields in the Pulsar Timing Array frequency band (2022).

Subramanian, K., "The origin, evolution and signatures of primordial magnetic fields," *Rep. Progr. Phys.* **79**, 076901 (2016).

$Header: /var/cvs/brandenb/tex/teach/COSMOMAG26/2_relic_gravitational_waves/notes.tex,v 1.6 2026/01/13 13:14:39 brandenb Exp $